# Multifunctional Effect of Fe Substitution in Na Layered Cathode Materials for Enhanced Storage Stability

Jehee Park, Kyojin Ku,* Jihyeon Gim, Seoung-bum Son, Heonjae Jeong, Lei Cheng, Hakim Iddir, Dewen Hou, Hui Xiong, Yuzi Liu, Eungje Lee,* and Christopher Johnson

Read Online

ACCESS | Metrics & More | Article Recommendations | Supporting Information

**ABSTRACT:** Developing stable cathode materials that are resistant to storage degradation is essential for practical development and industrial processing of Na-ion batteries as many sodium layered oxide materials are susceptible to hygroscopicity and instability upon exposure to ambient air. Among the various layered compounds, Fe-substituted O3-type $Na(Ni_{1/2}Mn_{1/2})_{1−x}Fe_xO_2$ materials have emerged as a promising option for high-performance and low-cost cathodes. While previous reports have noted the decent air-storage stability of these materials, the role and origin of Fe substitution in improving storage stability remain unclear. In this study, we investigate the air-resistant effect of Fe substitution in $O3-Na(Ni_{1/2}Mn_{1/2})_{1−x}Fe_xO_2$ cathode materials by performing systematic surface and structural characterizations. We find
that the improved storage stability can be attributed to the multifunctional effect of Fe substitution, which forms a surface protective layer containing an Fe-incorporated spinel phase and decreases the thermodynamical driving force for bulk chemical sodium extraction. With these mechanisms, Fe-containing cathodes can suppress the cascades of cathode degradation processes and better retain the electrochemical performance after air storage.

**KEYWORDS:** iron (Fe) cathode, Fe substitution, air storage, layered cathode, sodium-ion batteries
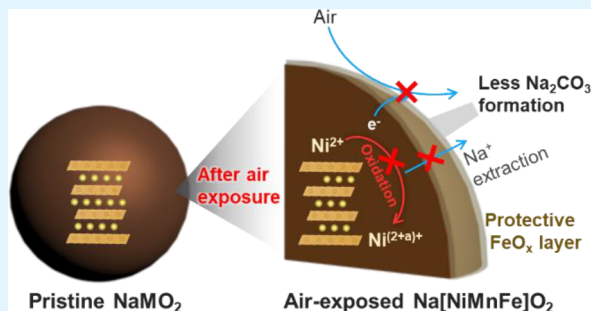
## 1. INTRODUCTION

Sodium-ion batteries have gained attention as a promising alternative to lithium-ion batteries for large-scale electrical energy storage systems due to the abundance, sustainability, and cost-effectiveness of sodium sources.[1] A variety of cathode materials have been explored to achieve high energy density and low-cost sodium-ion batteries, including layered Na transition metal oxide,[2,3] polyanion compounds,[4] and organic compounds.[5] Similar to the lithium-ion battery system, sodium layered oxide materials ($Na_xMO_2$) are being extensively investigated as the main group of cathode materials due to their high theoretical capacity, low cost, ease of synthesis, and scalability of production.[6−8] However, sodium layered oxide materials typically suffer from hygroscopic properties and air instability,[9] which can lead to undesirable cathode−air interfacial reactions. When layered oxide cathodes are exposed to a moist air atmosphere, the surface can undergo a hydrolysis reaction forming NaOH, which further converts to $NaHCO_3$ and $Na_2CO_3$ by $CO_2$ in air.[10] These surface impurity species cause several battery performance-related issues such as capacity loss, impedance increase, gas evolution, and electrolyte decomposition.[11,12] Furthermore, the alkaline nature of the residual sodium species promotes gelation of the cathode slurry, troubling the electrode fabrication process.[13] Therefore, designing air- and moisture-resistant sodium transition metal

oxide cathodes is critical for the manufacture and quality control of sodium-ion batteries.

One of the most common ways to preserve the pristine state of cathode materials is to coat the surface with a protective layer.[14] However, this approach often involves additional processes and costs. Particularly, it is not a trivial task to form a thin, conformal coating layer that acts as a physical barrier for surface degradation without impeding sodium transport, which is larger than lithium. An alternative strategy is to increase the cathode's chemical resistance to surface reactions involving ambient air molecules via bulk cation substitution or doping. There are several reports that demonstrate an improved storage stability of layered cathodes by adding cation substituents such as Cu,[15] Ti,[16] Mg,[17] Al,[18] Zr,[19] and Li.[20] For instance, Zheng et al. noted an enhanced storage stability of Cu-substituted $P2-Na_{2/3}Ni_{1/3−x}Cu_xMn_{2/3}O_2$ after being exposed to air up to 21 days, attributing the improvement to a shorter sodium interlayer distance and suppressed water
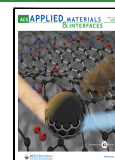
molecule insertion.[21] Yao et al. designed an air-stable cathode by substituting both $Cu^{2+}$ and $Ti^{4+}$ in an O3-Na-$Ni_{0.45}Cu_{0.05}Mn_{0.4}Ti_{0.1}O_2$ cathode that better maintains its crystal structure and electrochemical performance after air exposure.[22] Although this approach can be effective in achieving air-moisture stability, chemical tuning with redox-inactive elements has the drawback of lowering the energy density of cathode materials.

In this context, substitution with redox-active Fe provides a promising alternative, as it can offer both structural stability and redox activity.[23] It is known that proper Fe substitution in layered $Na_x(Ni,Mn)O_2$ can improve the electrochemical performance of the cathode material.[24−26] This beneficial effect has been attributed to several factors: (i) expanded transition metal layer distance increasing electron delocalization,[27] (ii) suppressed local structural distortion resulting in stable layer gliding and phase transition during cycling,[28] and (iii) reinforcement of layered structure facilitating Na diffusion and reversibility even at a highly desodiated state.[29] Furthermore, previous reports have noted that Fe substitution also improves storage stability, although the origin of the improvement and the role of Fe in controlling the hygroscopic property of layered compounds remain unclear.[27]

Herein, we systematically investigate the impact of Fe content on the air-storage properties of the O3-Na-$(Ni_{1/2}Mn_{1/2})_{1−x}Fe_xO_2$ cathodes. Compared to the Fe-free O3-NaNi$_{1/2}$Mn$_{1/2}$O$_2$ cathode that has poor air-storage properties, the solid solution compounds of the O3-Na-$(Ni_{1/2}Mn_{1/2})_{1−x}Fe_xO_2$ exhibit significantly improved surface and bulk structural stability under ambient air. We attribute this enhanced storage stability to the formation of a spinel-like surface layer and an elevated redox potential that raises the energy barrier for spontaneous sodium extraction and hydrolysis. Our findings open up new avenues for developing sodium layered cathode materials with superior electrochemical performance and ambient storage stability.

## 2. EXPERIMENTAL SECTION

**Synthesis.** $Ni_{1/2}Mn_{1/2}(OH)_2$ was prepared by the coprecipitation method in a continuously stirred tank reactor (CSTR), following a previous report.[30] Briefly, $NiSO_4·6H_2O$ and $MnSO_4·H_2O$ (Sigma-Aldrich) were used as starting materials, and the metal−solution was fed into the CSTR with aqueous NaOH and $NH_4OH$ as a chelating agent. The precipitated $[Ni_{0.5}Mn_{0.5}](OH)_2$ precursor powder was obtained by filtering, washing, and drying. $Na(Ni_{1/2}Mn_{1/2})_{1−x}Fe_xO_2$ powder samples were synthesized by the solid-state reaction of $Ni_{1/2}Mn_{1/2}(OH)_2$, $Fe_2O_3$ (Sigma-Aldrich), and $Na_2CO_3$ (5% excess condition; Sigma-Aldrich). The precursor powders were mixed using a mortar and pestle and heat-treated at 850 °C for 24 h in air. The calcined powder was retrieved from the furnace without a cooling process and transferred into an Ar-filled glovebox to limit exposure to ambient air (pristine sample). For the aged samples, approximately 1 g of the pristine powder was placed in a plastic weighing boat and exposed to ambient air up to 5 days.

**Materials Characterization.** The crystal structure of the cathode samples was analyzed by high-resolution synchrotron X-ray diffraction (SXRD) at beamline 11ID-C (wavelength = 0.1173 Å) of the Advanced Photon Source (APS, Argonne National Laboratory). The collected 2D diffraction patterns were calibrated with a $CeO_2$ standard and then integrated into 1D patterns using the GSAS II software. The powder morphology was observed using a scanning electron microscope (SEM) with a JEOL JCM-6000 plus. Transmission electron microscopy (TEM) measurements were performed on the JEOL JEM2100F microscope with an accelerating voltage of 200 kV. The TEM samples were prepared by directly spreading the

powder samples on a Cu grid coated with an amorphous carbon support film. Thermogravimetric analysis (TGA) was collected using a Netzsch STA 449 F3 Jupiter instrument at a scan rate of 5 °C/min in the temperature range of room temperature to 800 °C under an Ar flow. X-ray photoelectron spectroscopy (XPS) analysis was performed with a PHI 5000 VersaProbe II System (Physical Electronics). The spectra were collected using an Al Kα radiation ($hν$ = 1486.6 eV) beam (100 μm, 25 W), with $Ar^+$ and electron beam sample neutralization in the Fixed Analyzer Transmission mode. XPS spectra were aligned with the carbon black component in the C 1s spectra at 284.8 eV.

**Electrochemical Test.** The electrochemical properties of Na-$(Ni_{1/2}Mn_{1/2})_{1−x}Fe_xO_2$ were tested by using 2032-type coin cells. The electrode slurry was prepared by mixing the active material, Super P carbon (C45, Timcal), and poly(vinylidene fluoride) (PVDF, Solvay 5130) binder with an 8:1:1 weight ratio and using N-methyl-2-pyrrolidone (NMP, Sigma-Aldrich) as solvent. The slurry was cast on aluminum foil and dried in a vacuum oven. Typical active material loading was ∼3.5 mg cm$^{−2}$. The coin cell was assembled in a high purity argon-filled glovebox. Sodium metal foil was used as the anode, glass fiber filter (Whatman, F grade) as the separator, and 1 M $NaPF_6$ (Stella Chemifa, Japan) in propylene carbonate (PC, Sigma-Aldrich) with 2 wt % of fluoroethylene carbonate (FEC, Sigma-Aldrich) as the electrolyte. The electrochemical tests were performed with a current density of 10 mA/g in the voltage range 2−3.8 V by using a battery cycler system (Maccor, Inc.) at room temperature. Electrochemical impedance spectroscopy (EIS) was measured by a potentiostat (VSP-300, Biologic) in the frequency range from 200 kHz to 10 mHz.

**DFT Calculation.** We used first-principles density functional theory (DFT) simulations as implemented in the Vienna *Ab Initio* Simulation Package (VASP).[31,32] The calculations were performed using the Perdew−Burke−Ernzerhof (PBE) exchange-correlation functional[33] and the projector augmented wave (PAW) method.[34] The plane wave energy cutoff was chosen to be 520 eV. We used Gamma-centered Monkhorst−Pack k-point sampling, which will be discussed in more detail later. We relaxed all of the atoms until the forces converged to less than 0.02 eV/Å for atoms. To correct the charge localization on transition metals (Ni, Mn, and Fe atoms), we used the Dudarev's approach of $U − J(U_{eff})$ parameter.[35] The optimal $U_{eff}$ value needs empirical tests and can differ between compounds depending on their properties.[36] We set the $U_{eff}$ values to 6.0 eV for Ni, 4.0 eV for Mn, and 4.5 eV for Fe, following a previous study.[27,37,38] All calculations were spin-polarized, and we tested several initial spin states for the transition metals to reach the most stable electronic structure solution. Theoretical voltage ($V$) was the open-circuit potential (V vs Na) and is given by

$$V = \{E[Na_{y_2}(Ni_{0.5}Mn_{0.5})_{1−x}Fe_xO_2]$$
$$− [Na_{y_1}(Ni_{0.5}Mn_{0.5})_{1−x}Fe_xO_2] − (y_2 − y_1)E[Na]\}/(y_2 − y_1)$$

where $E$ is the total energy of the compounds by DFT calculations, $x$ is the composition of Fe ions, and $y_1$ and $y_2$ are the compositions of Na ions intercalated.[37] To establish the correlation between the voltage ($V$) and Fe fraction, we studied five different Fe compositions ($x$ = 0, 1/3, 1/2, 2/3, and 1). Different supercell sizes were used to model different $x$ values to achieve the desired Fe ratios. When $x$ = 0, we used 2 × 2 × 1 supercells including 48 atoms (6 Ni, 6 Mn, 12 Na, and 24 O) with a 3 × 3 × 1 k-point mesh. For $x$ = 1/3, we used 3 × 3 × 1 supercells including 108 atoms (27 Na, 9 Ni, 9 Mn, 9 Fe, and 54 O) with a 2 × 2 × 1 k-point mesh. For $x$ = 1/2, we used 2 × 2 × 1 supercells including 48 atoms (12 Na, 3 Ni, 3 Mn, 6 Fe, and 24 O) with a 3 × 3 × 1 k-point mesh. For $x$ = 2/3, we used 2 × 3 × 1 supercells including 72 atoms (18 Na, 3 Ni, 3 Mn, 12 Fe, and 36 O) with a 3 × 2 × 1 k-point mesh. For $x$ = 1, we used 2 × 2 × 1 supercells including 48 atoms (12 Fe, 12 Na, and 24 O) with a 3 × 3 × 1 k-point mesh. We tested various Fe positions for each composition, until the most stable structure was identified. The representative structures are shown in Figure S6.
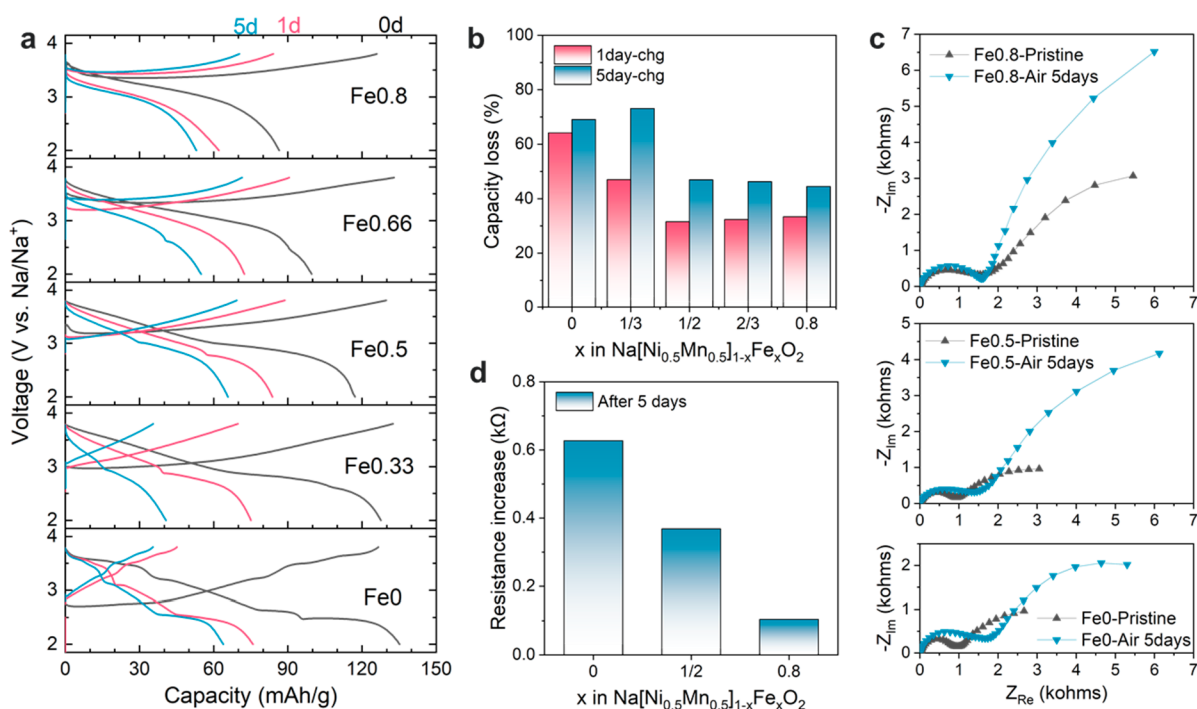
**Figure 1.** Electrochemical characterization of pristine and air-exposed $Na(Ni_{0.5}Mn_{0.5})_{1-x}Fe_xO_2$ ($x = 0$, 1/3, 1/2, 2/3, and 0.8) cathodes. (a) Initial charge−discharge voltage profiles at a current density of 10 mA/g in a voltage range of 2−3.8 V. (b) Initial charge capacity loss after air exposure for different Fe compositions. (c) Nyquist plots of pristine and 5-day-exposed Fe0, Fe0.5, and Fe0.8 cathodes. (d) Interfacial resistance increase after 5-day air exposure as a function of Fe composition.

## 3. RESULTS AND DISCUSSION

$Na(Ni_{1/2}Mn_{1/2})_{1-x}Fe_xO_2$ ($x = 0$, 1/3, 0.5, 2/3, and 0.8, denoted as Fe0, Fe0.33, Fe0.5, Fe0.66, and Fe0.8, respectively) was successfully synthesized via the solid-state method. The powder SXRD data indicated a well-crystallized O3-type layered structure with an $R\bar{3}m$ space group, consistent with the reported crystal structure of $Na(Ni_{1/2}Mn_{1/2})_{1-x}Fe_xO_2$ (Figure S1a). No additional diffraction peaks were observed, except for the Fe0.8 sample, which included a small amount of $\beta$-$NaFeO_2$. The lattice parameters were calculated using the Pawley refinement method. The results show a linear relationship between the lattice constants and Fe content (Figure S1b), indicating the formation of solid solution $Na(Ni_{1/2}Mn_{1/2})_{1-x}Fe_xO_2$ compounds.[25] Figure S1c shows the electrochemical charge−discharge profiles of Na-$(Ni_{1/2}Mn_{1/2})_{1-x}Fe_xO_2$ cycled at a current density of 10 mA/g between 2 and 3.8 V. These cathode materials were cycled within mild voltage windows (up to 3.8 V vs $Na/Na^+$) because operation up to higher voltage to access additional capacity is generally avoided due to severe interfacial and structural degradation.[39−41] The Fe-free sample (i.e., Fe0) exhibits multiple voltage steps that are associated with phase transitions and Na/vacancy orderings. In contrast, the Fe-containing cathodes show smoother voltage profiles. This transition is commonly attributed to enhanced electron delocalization, which suppresses the formation of unstable monoclinic intermediate phases.[27]

**Electrochemical Performance Degradation.** To assess air-storage stability, we compared the decline in electrochemical sodium storage capability by testing the cathode powders exposed to varied lengths of ambient air exposure. Figure 1a shows the initial charge−discharge voltage profiles of the pristine (black), 1-day (red), and 5-day (blue) air-exposed

$Na(Ni_{1/2}Mn_{1/2})_{1-x}Fe_xO_2$ electrodes. The Fe-free and low-Fe cathodes (Fe0 and Fe0.33) demonstrate a significant reduction in the initial charge capacity after exposure, whereas the high-Fe cathodes (Fe0.5, Fe0.66, and Fe0.8) maintain their capacity better even after prolonged exposure to air. Figure 1b illustrates the percentage decrease in the initial charge capacity upon air exposure as a function of the Fe composition. In contrast to the low-Fe cathodes, which experienced a reduction in charge capacity of over 60% following air exposure, the high-Fe cathodes exhibit only about 30% and a below 50% capacity reduction after 1 and 5 days of air exposure, respectively. Notably, the low-Fe cathodes show a significant increase in the first cycle Coulombic efficiency values upon exposure to ambient air (e.g., from 107% to 180% for Fe0 and from 94% to 116% for Fe0.33 after 5 days of exposure), implying that considerable amounts of sodium ions were extracted from the cathodes during the storage, which will be corroborated by the physicochemical analysis results described in the following sections.

The low-Fe cathodes also showed a significant rise in the impedance after being exposed to air. Figure 1c compares EIS data collected before (black) and after (blue) air exposure. For Fe0, the semicircle at the high-frequency range, which corresponds to the interfacial and charge transfer resistance (equivalent circuit in Figure S2), significantly increasing from 0.9 kΩ to 1.5 Ω after exposure (corresponding to a 70% increase, Figure 1d). In contrast, the Fe0.5 and Fe0.8 cathodes have only a 43% and 7% increase in interfacial resistance, respectively. The decreased interfacial impedance rise for the Fe-substituted cathodes implies suppressed surface side reaction and degradation.

**Spontaneous Sodium Extraction and Surface Deterioration.** In light of the electrochemical testing results, a physicochemical analysis was conducted to examine the bulk
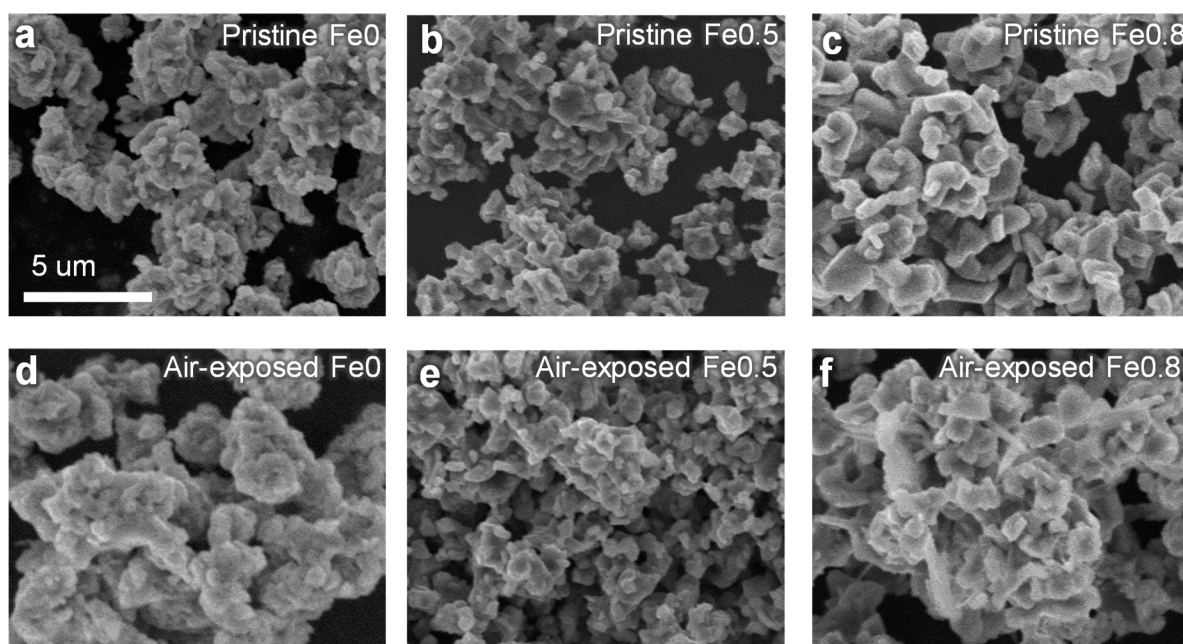
**Figure 2.** SEM Images of $Na(Ni_{0.5}Mn_{0.5})_{1-x}Fe_xO_2$ ($x$ = 0, 1/3, 1/2, 2/3, and 0.8) cathodes. (a−c) Fe0, Fe0.5, and Fe0.8 cathodes as synthesized. (d−f) Fe0, Fe0.5, and Fe0.8 cathodes after exposure to air for 5 days.
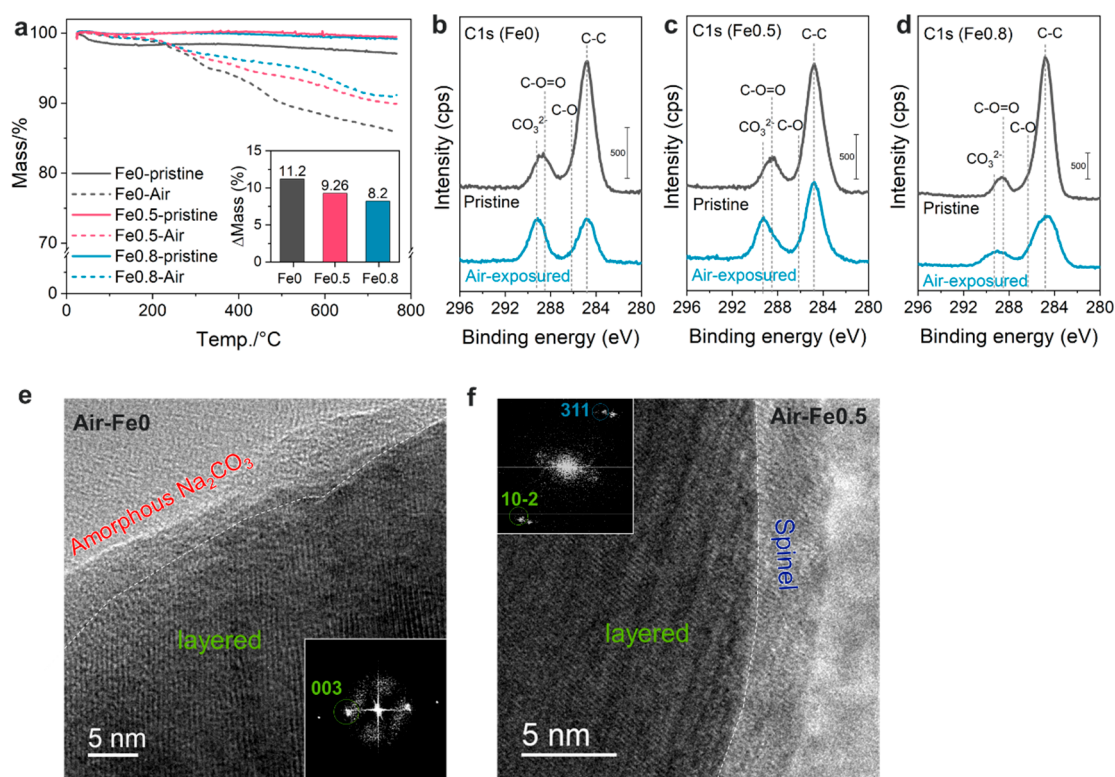


**Figure 3.** Characterization of air-exposed $Na(Ni_{0.5}Mn_{0.5})_{1-x}Fe_xO_2$ ($x$ = 0, 1/2, and 0.8) cathodes. (a) TGA analysis and (b−d) XPS C 1s spectra of Fe0, Fe0.5, and Fe0.8 cathodes before and after air exposure for 5 days. (e, f) HRTEM images and corresponding FFT patterns (inset) of air-exposed Fe0 and Fe0.5 cathodes after being exposed to air for 5 days.

and surface degradation of the aged cathode particles. The improved surface stability with Fe substitution was observed from SEM analysis, by which overall surface morphological characteristics were probed. In Figure 2, all the pristine Fe0, Fe0.5, and Fe0.8 cathode materials have similar aggregated particle morphology. After 5 days of air exposure, the surface of

Fe0 particles was almost completely covered by a thick layer of residual sodium species, whereas the Fe-containing cathodes (Fe0.5 and Fe0.8) retained their original surface morphology.

The levels of surface residual sodium species determined by TGA were consistent with the electrochemistry and SEM results. Figure 3a plots the weight loss of the air-exposed
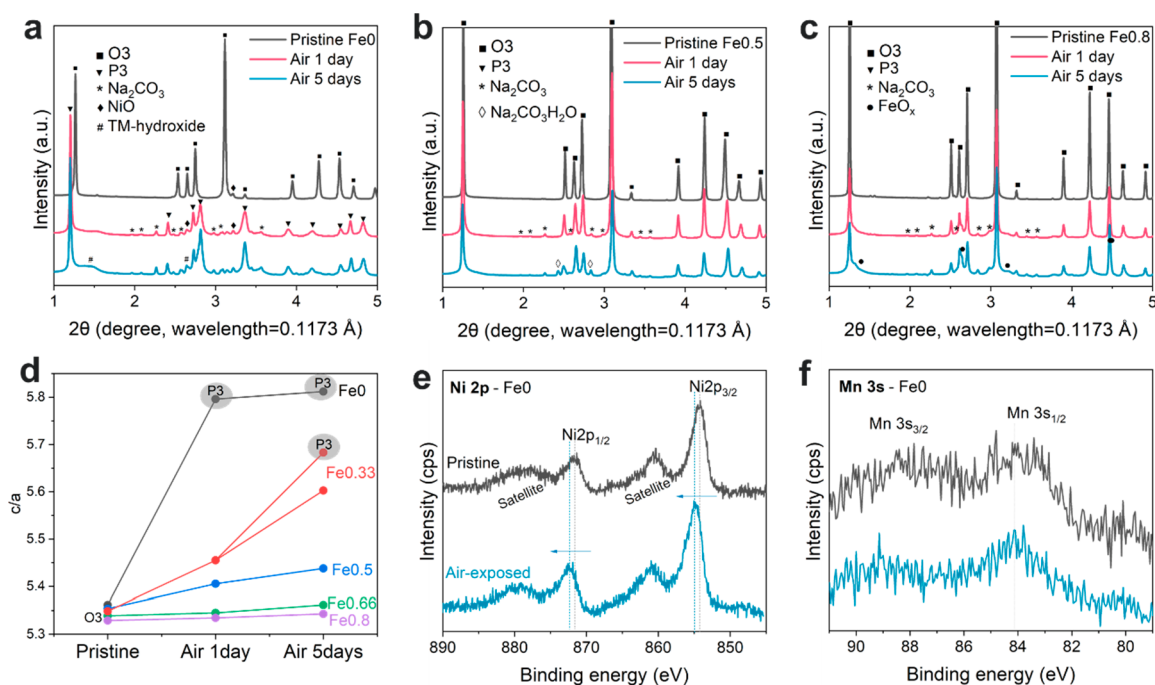
**Figure 4.** Structural characterization of air-exposed $Na(Ni_{0.5}Mn_{0.5})_{1-x}Fe_xO_2$ ($x$ = 0, 1/3, 1/2, 2/3, and 0.8) cathodes. (a–c) SXRD patterns of Fe0, Fe0.5, and Fe0.8 cathodes after being exposed to air for 1 and 5 days. (d) Lattice parameters of the cathodes after air exposure. (e) XPS Ni 2p spectra and (f) Mn 3s spectra of pristine Fe0 cathode and after being exposed for 5 days.

cathode powder sample during heating to 800 °C under an Ar flow. After the slight weight loss below 200 °C that can be associated with the evaporation of physically absorbed $H_2O$, the thermal decomposition of residual sodium surface contaminants such as NaOH and $Na_2CO_3$ results in the large weight loss at the higher temperature range above 200 °C. The weight loss (wt %) in the entire temperature range was calculated, as shown in the inset of Figure 3a, which indicates an enhanced resistance against air/moisture exposure in high-Fe cathodes. From room temperature to 750 °C, Fe0 had 11.2% weight loss, and the value decreased to 9.7% and 8.2% for Fe0.5 and Fe0.8, respectively.

The chemical nature of residual Na species on the air-exposed $Na(Ni_{1/2}Mn_{1/2})_{1-x}Fe_xO_2$ cathode surface was examined through XPS analyses. Figure 3b–d represents the C 1s spectra of pristine (black) and air-exposed (blue) cathodes. Carbonaceous species were observed on the pristine cathode surface, which could have resulted from adventitious contamination during the material transfer process. After 5 days of air exposure, the metal carbonate peak $(CO_3^{2-})$ at ~289 eV was found to grow significantly for the Fe0 cathode, and the intensity of this peak increased relatively much higher than that of the C−C peak (Figure 3b). The XPS results indicate the formation of a large amount of $Na_2CO_3$ residual sodium specie on the surface of the Fe0 cathode. Although the presence of the NaOH species cannot be determined unambiguously due to the similar O 1s binding energies (~531.3 eV) for both NaOH and $Na_2CO_3$, we believe $Na_2CO_3$ was the major constituent of the residual sodium layer, as the NaOH to $Na_2CO_3$ conversion ($2NaOH + CO_2 \rightarrow Na_2CO_3 + H_2O$) is facile under an air-conditioned laboratory room environment. In contrast to Fe0, a much suppressed increase in the $CO_3^{2-}$ peak after air exposure (relative to the C−C peak intensity) was observed for the high-Fe cathodes (Figures 3c,d,

and S3), which further confirms the suppression of carbonate species formation in the high-Fe cathodes.

The air-exposed surfaces of the Fe0 and Fe0.5 cathodes were further examined by high-resolution TEM (HRTEM). In Figure 3e, the surface of Fe0 is covered with an amorphous layer, which can be attributed to a residual sodium species.[42] It appears that the residual sodium layer does not conformally passivate the cathode surface but rather accumulates on local hot areas, where continuous Na loss and surface layer growth occur upon prolonged air exposure. For the air-exposed Fe0.5 sample, the HRTEM image also shows the formation of a poorly crystalline surface layer, which is indexed as a spinel-type phase (Figure 3f). The corresponding Fast Fourier transformation (FFT) pattern shows the (311) plane of the $M_3O_4$ ($Fd\bar{3}m$) spinel structure and the (10−2) plane of the original layered structure. Noting that Fe migration into the Na layer can occur during desodation in Fe-containing layered oxides,[29] it is presumed that the surface region where the air/moisture reaction and sodium $Na^+$ extraction take place undergoes a structural transition to a spinel-like surface phase. In comparison to the amorphous residual sodium surface layer, the spinel-type layer may passivate and stabilize the cathode surface, effectively suppressing surface side reactions, bulk $Na^+$ extraction, and impedance growth.

**Bulk Structural Transition.** In addition to the surface degradation, the bulk structural changes in the air-exposed particles were investigated by SXRD analysis. Figure 4a–c presents SXRD patterns of the pristine (black), 1-day (red), and 5-day (blue) exposed powder samples of Fe0, Fe0.5, and Fe0.8, respectively. All pristine cathode structures are indexed to the α-NaFeO2 phase (space group R3-m), which is an O3-type layered structure with stoichiometric Na content. After 1 day of air exposure, Fe0 exhibited the emergence of new peaks that are indexed to $Na_2CO_3$ and NiO impurity products. With an increasing exposure time to 5 days, the intensity of the
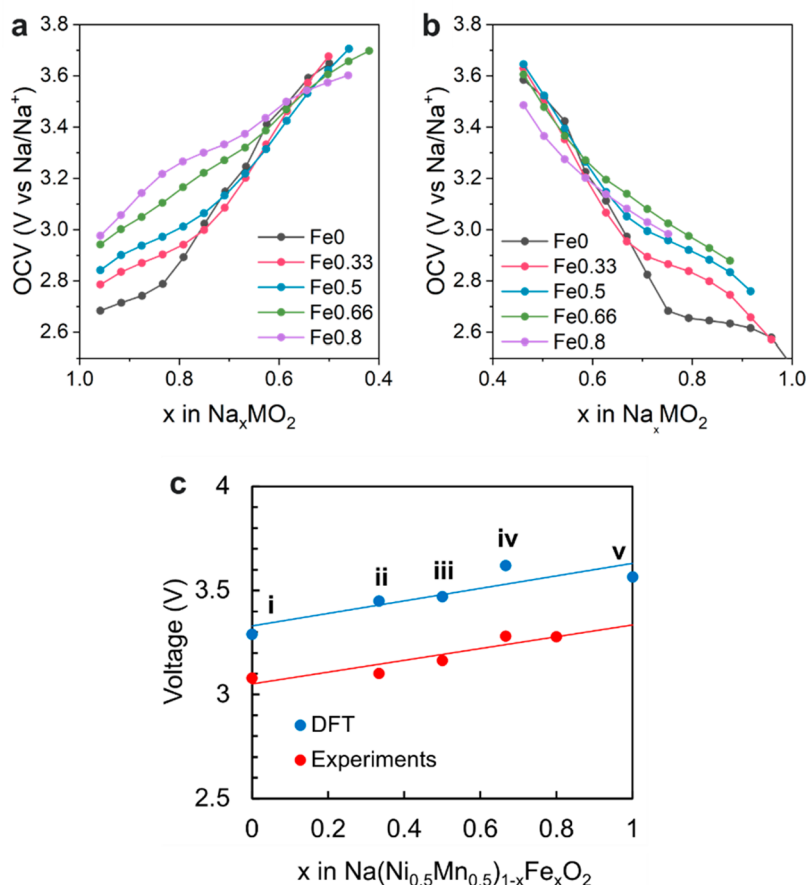
**Figure 5.** (a, b) OCV plot of $Na(Ni_{0.5}Mn_{0.5})_{1-x}Fe_xO_2$ during charging and discharging at a current density of 10 mA/g in the voltage range 2−3.8 V. (c) Theoretical voltages calculated by DFT for the O3-type $Na(Ni_{0.5}Mn_{0.5})_{1-x}Fe_xO_2$ cathodes at various Fe compositions ($x$) and a comparison with experimental potentials during charging and discharging characterization.

impurity peaks increased at the expense of the main layered phase. Interestingly enough, the SXRD result shows that the bulk structure of Fe0 completely transforms from the pristine O3-type layered phase to the P3-type phase only after 1 day of air exposure; the shift of the (003) peak toward a lower $2\theta$ angle direction and the emergence of the (015) peak (3.36°) at the expense of the (104) peak (3.11°) are indicative of P3 phase formation. Given that the P3-type layered structure is stabilized in sodium-deficient $Na_{1-x}MO_2$ compositions, the observed O3 to P3 phase transition suggests that considerable amounts of sodium extraction occurred spontaneously during the air storage of the Fe0 cathode sample. In stark contrast, the Fe0.5 and Fe0.8 cathodes retained the O3-layered structure even after 5 days of air exposure, proving much suppressed sodium extraction and enhanced surface stability. The impact of Fe content in stabilizing the pristine O3 layered structure upon air exposure is displayed in Figure 4d (see also Figure S4d,e), where the high-Fe cathodes exhibit insignificant lattice parameter changes compared to the low-Fe compounds, which have a substantial variation as well as P3 transformation. It is also noteworthy that a careful examination of the 5-day-exposed Fe0.8 pattern reveals broad but noticeable reflections at 1.3°, 2.7°, and 3.2° (marked with black dots in Figure 4c), which are tentatively assigned to an Fe-based spinel-like phase.

It is quite surprising that a complete bulk phase transition from the O3 to P3 structure can take place spontaneously after only a day of air exposure, even with the large secondary particles that we tested. While such an extensive bulk degradation was unexpected, it is encouraging to discover that Fe substitution is highly effective in suppressing chemical desodiation. In order to maintain charge neutrality without decomposing the layered structure, such as through oxygen loss, chemical sodium extraction must be accompanied by either transition metal oxidation $(Na_{1-x}MO_2)$ or proton insertion without oxidizing transition metal cations $(Na_{1-x}H_xMO_2)$.[43]

To investigate the major charge compensation mechanism for chemical sodium extraction during air storage, the oxidation states of transition metal cations were analyzed by XPS. Figure 4e,f presents the XPS Ni 2p and Mn 3s spectra of the Fe0 cathode before and after exposure to air for 5 days (measurement depth of less than ∼5 nm). Following air exposure, the Ni $2p_{3/2}$ spectra and their satellite peaks shifted to higher binding energy, indicating the oxidation of Ni on the surface $(Ni^{(3+a)+})$, whereas Mn retained the pristine oxidation state of $Mn^{4+}$. A similar, yet less pronounced, trend was observed in the Fe0.5 cathode, as shown in Figure S5. These observations suggest that chemical desodiation due to air exposure is largely, if not completely, compensated by Ni oxidation, and the Fe substitution effectively suppresses the oxidation behavior, which can also be interpreted as a reduction in desodiation and surface side reactions.

In addition to the Fe-incorporated spinel layer at the surface region, which may serve as a physical barrier to impede the
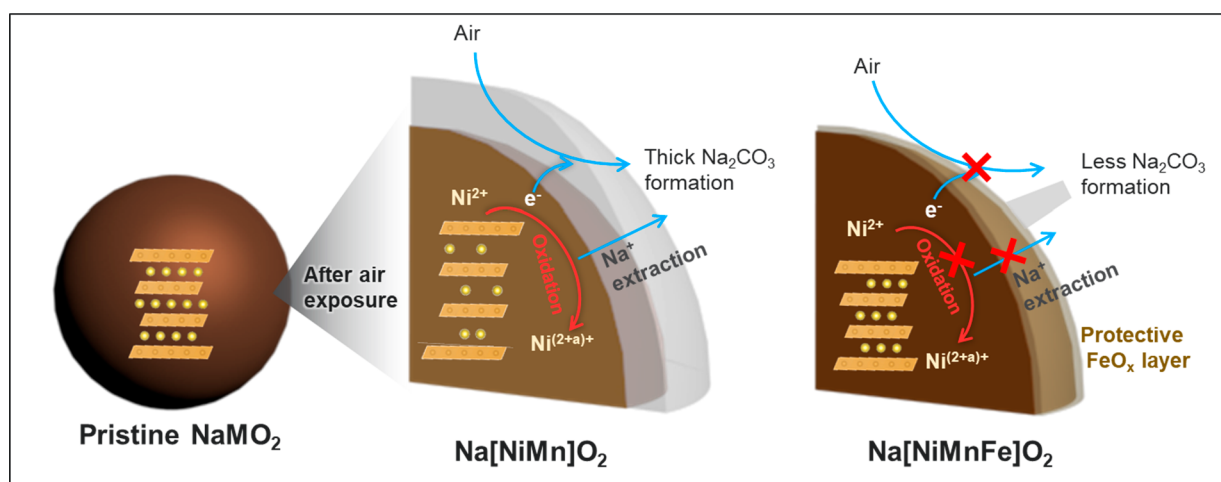
**Figure 6.** Schematic diagram of the surface degradation mechanism of Na[NiMn]O$_2$ and Na[NiMnFe]O$_2$ by air exposure.

progression of surface side reactions, it is evident that Fe substitution also enhances the thermodynamic barrier for the chemical desodiation process. Because the chemical desodiation reaction is a crucial step in both surface and bulk degradation events, minimizing the thermodynamic driving force for this reaction makes for a highly effective and fundamental approach for air-stable cathodes. Adding Fe to Na(Ni$_{1/2}$Mn$_{1/2}$)$_{1-x}$Fe$_x$O$_2$ cathodes can control their work potential, which in turn determines the thermodynamic driving force for desodiation. Figures 5a and 5b plot the open-circuit voltages (OCV) measured during the charge and discharge of Na(Ni$_{1/2}$Mn$_{1/2}$)$_{1-x}$Fe$_x$O$_2$. The OCV values at various states of charge (SOC) provide important thermodynamic information about the electrode material after relaxation of kinetic processes. These values characterize the energy difference before and after sodium ion extraction. During the initial stage of charging, where Ni redox is responsible for electrochemical sodium deintercalation, the OCV of Na(Ni$_{1/2}$Mn$_{1/2}$)$_{1-x}$Fe$_x$O$_2$ increases with the Fe concentration. This indicates that the Ni oxidation potential is increased due to the influence of the multicompositional effect. When Fe with a larger ionic radius is substituted for Ni$_{1/2}$Mn$_{1/2}$, it stabilizes the layered structure and enhances electron delocalization. This bring out the increased ionicity between Ni and O, leading to an elevation of redox potential.[44,45] This result is further supported by DFT calculations, as shown in Figure 5c, where the theoretical voltage of the cathodes increases as the Fe content increases. Therefore, the improved air-storage stability of the high-Fe compounds can also be attributed to their higher oxidation barrier, which suppresses the Na extraction from the bulk layered structure and the subsequent cascades of surface degradation.

**Multifunctional Effect of Fe Substitution.** Figure 6 summarizes the effect of Fe substitution on the storage stability of Na(Ni$_{1/2}$Mn$_{1/2}$)$_{1-x}$Fe$_x$O$_2$ cathodes under ambient conditions. When the cathode is exposed to air, a cathode−air interfacial side reaction occurs, inducing desodiation, a phase transition into a Na-deficient layered structure, and surface layer formation. However, Fe substitution improves the air storage stability by its multifunctional role: (i) spontaneous formation of a stable spinel surface layer to physically protect cathode materials and (ii) tuning of the oxidation potential by providing a higher oxidation potential to thermodynamically stabilize materials. From the viewpoint of designing sodium layered oxide materials (Na$_x$MO$_2$), the introduction of Fe into the MO$_2$ layer provides a multifunctional effect that stabilizes the electrochemistry by suppressing undesirable phase transitions and elevating the operating voltage. It also provides enhanced air stability by the self-passivation behavior. These critical roles and synergetic effects of an Fe substituent for performance and storage issues could be considered in the design of high-performance and stable layered cathode materials for Na-ion batteries.

## 4. CONCLUSION

In summary, we confirmed the beneficial effects of Fe substitution in Na(Ni$_{0.5}$Mn$_{0.5}$)$_{1-x}$Fe$_x$O$_2$ with regard to the air storage properties at different Fe concentrations. The high-Fe cathodes showed reduced performance degradation and suppressed surface and bulk structural deterioration compared to Fe-free and low-Fe cathodes, which exhibited poor air-storage properties. The improved air stability was attributed to the multifunctional effects of Fe that are the spontaneous formation of a stable spinel surface layer to physically protect the cathode surface and the elevation of the cathode working potential to reduce the thermodynamic driving force for chemical sodium extraction from the layered structure. These findings highlight the critical role and synergetic effect of Fe substitution for improved performance and storage properties. This work provides a new strategy for designing "ambient-air-resistant" sodium cathode materials using redox-active multifunctional substituents.

## ■ ASSOCIATED CONTENT

### ⓢ Supporting Information

The Supporting Information is available free of charge at https://pubs.acs.org/doi/10.1021/acsami.3c07068.

> Additional figures including XRD patterns, electrochemical result, XPS analysis, and DFT calculation results (PDF)

## ■ AUTHOR INFORMATION

### Corresponding Authors

**Kyojin Ku** − *Department of Materials Science and Engineering, Hanbat National University, Daejeon 34158, Republic of Korea;* Email: kjku@hanbat.ac.kr

**Eungje Lee** − *Chemical Sciences and Engineering Division, Argonne National Laboratory, Lemont, Illinois 60439, United States;* ⊙ orcid.org/0000-0003-3647-1595; Email: eungje.lee@anl.gov

**Authors**

**Jehee Park** − *Chemical Sciences and Engineering Division, Argonne National Laboratory, Lemont, Illinois 60439, United States*

**Jihyeon Gim** − *Chemical Sciences and Engineering Division, Argonne National Laboratory, Lemont, Illinois 60439, United States;* ⊙ orcid.org/0000-0002-4171-3707

**Seoung-bum Son** − *Chemical Sciences and Engineering Division, Argonne National Laboratory, Lemont, Illinois 60439, United States;* ⊙ orcid.org/0000-0002-3723-6186

**Heonjae Jeong** − *Materials Science Division, Argonne National Laboratory, Lemont, Illinois 60439, United States*

**Lei Cheng** − *Materials Science Division, Argonne National Laboratory, Lemont, Illinois 60439, United States;* ⊙ orcid.org/0000-0002-3902-1680

**Hakim Iddir** − *Chemical Sciences and Engineering Division, Argonne National Laboratory, Lemont, Illinois 60439, United States;* ⊙ orcid.org/0000-0001-5285-6474

**Dewen Hou** − *Micron School of Materials Science and Engineering, Boise State University, Boise, Idaho 83725, United States; Center for Nanoscale Materials, Argonne National Laboratory, Lemont, Illinois 60439, United States*

**Hui Xiong** − *Micron School of Materials Science and Engineering, Boise State University, Boise, Idaho 83725, United States;* ⊙ orcid.org/0000-0003-3126-1476

**Yuzi Liu** − *Center for Nanoscale Materials, Argonne National Laboratory, Lemont, Illinois 60439, United States;* ⊙ orcid.org/0000-0002-8733-1683

**Christopher Johnson** − *Chemical Sciences and Engineering Division, Argonne National Laboratory, Lemont, Illinois 60439, United States;* ⊙ orcid.org/0000-0003-4357-6889

Complete contact information is available at:
https://pubs.acs.org/10.1021/acsami.3c07068

**Notes**
The authors declare no competing financial interest.

■ **REFERENCES**

(1) Slater, M. D.; Kim, D.; Lee, E.; Johnson, C. S. Sodium-Ion Batteries. *Adv. Funct. Mater.* **2013**, *23*, 947−958.

(2) Han, M. H.; Gonzalo, E.; Singh, G.; Rojo, T. A Comprehensive Review of Sodium Layered Oxides: Powerful Cathodes for Na-Ion Batteries. *Energy Environ. Sci.* **2015**, *8*, 81−102.

(3) Kubota, K.; Yabuuchi, N.; Yoshida, H.; Dahbi, M.; Komaba, S. Layered Oxides as Positive Electrode Materials for Na-Ion Batteries. *MRS Bull.* **2014**, *39*, 416−422.

(4) Jin, T.; Li, H.; Zhu, K.; Wang, P.-F.; Liu, P.; Jiao, L. Polyanion-Type Cathode Materials for Sodium-Ion Batteries. *Chem. Soc. Rev.* **2020**, *49*, 2342−2377.

(5) Zhang, H.; Gao, Y.; Liu, X.-H.; Yang, Z.; He, X.-X.; Li, L.; Qiao, Y.; Chen, W.-H.; Zeng, R.-H.; Wang, Y.; Chou, S.-L. Organic Cathode Materials for Sodium-Ion Batteries: From Fundamental Research to Potential Commercial Application. *Adv. Funct. Mater.* **2022**, *32*, No. 2107718.

(6) Kubota, K.; Komaba, S. Practical Issues and Future Perspective for Na-Ion Batteries. *J. Electrochem. Soc.* **2015**, *162*, A2538.

(7) Rudola, A.; Rennie, A. J. R.; Heap, R.; Meysami, S. S.; Lowbridge, A.; Mazzali, F.; Sayers, R.; Wright, C. J.; Barker, J. Commercialisation of High Energy Density Sodium-Ion Batteries: Faradion's Journey and Outlook. *J. Mater. Chem. A* **2021**, *9*, 8279−8302.

(8) Tapia-Ruiz, N.; Armstrong, A. R.; Alptekin, H.; Amores, M. A.; Au, H.; Barker, J.; Boston, R.; Brant, W. R.; Brittain, J. M.; Chen, Y.; Chhowalla, M.; Choi, Y.-S.; Costa, S. I. R.; Crespo Ribadeneyra, M.; Cussen, S. A.; Cussen, E. J.; David, W. I. F.; Desai, A. V.; Dickson, S. A. M.; Eweka, E. I.; Forero-Saboya, J. D.; Grey, C. P.; Griffin, J. M.; Gross, P.; Hua, X.; Irvine, J. T. S.; Johansson, P.; Jones, M. O.; Karlsmo, M.; Kendrick, E.; Kim, E.; Kolosov, O. V.; Li, Z.; Mertens, S. F. L.; Mogensen, R.; Monconduit, L.; Morris, R. E.; Naylor, A. J.; Nikman, S.; O'Keefe, C. A.; Ould, D. M. C.; Palgrave, R. G.; Poizot, P.; Ponrouch, A.; Renault, S.; Reynolds, E. M.; Rudola, A.; Sayers, R.; Scanlon, D. O.; Sen, S.; Seymour, V. R.; Silván, B.; Sougrati, M. T.; Stievano, L.; Stone, G. S.; Thomas, C. I.; Titirici, M.-M.; Tong, J.; Wood, T. J.; Wright, D. S.; Younesi, R. 2021 Roadmap for Sodium-Ion Batteries. *Journal of Physics: Energy* **2021**, *3*, No. 031503.

(9) Zhang, Y.; Zhang, R.; Huang, Y. Air-Stable $Na_xTMO_2$ Cathodes for Sodium Storage. *Frontiers in Chemistry* **2019**, *7*, 335.

(10) Wang, P. F.; You, Y.; Yin, Y. X.; Guo, Y. G. Layered Oxide Cathodes for Sodium-Ion Batteries: Phase Transition, Air Stability, and Performance. *Adv. Energy Mater.* **2018**, *8* (8), No. 1701912.

(11) Choi, K. H.; Liu, X.; Ding, X.; Xia, Y.; Li, Q. Impact of Gelation in Nickel-Rich Ternary Lithium-Ion Batteries. *Ionics* **2021**, *27* (12), 5159−5166.

(12) Bi, Y.; Li, Q.; Yi, R.; Xiao, J. To Pave the Way for Large-Scale Electrode Processing of Moisture-Sensitive Ni-Rich Cathodes. *J. Electrochem. Soc.* **2022**, *169*, No. 020521.

(13) Seong, W. M.; Kim, Y.; Manthiram, A. Impact of Residual Lithium on the Adoption of High-Nickel Layered Oxide Cathodes for Lithium-Ion Batteries. *Chem. Mater.* **2020**, *32* (22), 9479−9489.

(14) Guan, P.; Zhou, L.; Yu, Z.; Sun, Y.; Liu, Y.; Wu, F.; Jiang, Y.; Chu, D. Recent Progress of Surface Coating on Cathode Materials for High-Performance Lithium-Ion Batteries. *J. Energy Chem.* **2020**, *43*, 220−235.

(15) Zheng, L.; Li, J.; Obrovac, M. Crystal Structures and Electrochemical Performance of Air-Stable $Na_{2/3}Ni_{1/3−x}Cu_xMn_{2/3}O_2$ in Sodium Cells. *Chem. Mater.* **2017**, *29* (4), 1623−1631.

(16) Tan, L.; Wu, Q.; Liu, Z.; Chen, Q.; Yi, H.; Zhao, Z.; Song, L.; Zhong, S.; Wu, X.; Li, L. Ti-Substituted O3-Type Layered Oxide Cathode Material with High-Voltage Stability for Sodium-Ion Batteries. *J. Colloid Interface Sci.* **2022**, *622*, 1037−1044.

(17) Zhou, Y.-N.; Wang, P.-F.; Zhang, X.-D.; Huang, L.-B.; Wang, W.-P.; Yin, Y.-X.; Xu, S.; Guo, Y.-G. Air-Stable and High-Voltage

Layered P3-Type Cathode for Sodium-Ion Full Battery. *ACS Appl. Mater. Interfaces* **2019**, *11* (27), 24184−24191.

(18) Li, X.; Shen, X.; Zhao, J.; Yang, Y.; Zhang, Q.; Ding, F.; Han, M.; Xu, C.; Yang, C.; Liu, H.; Hu, Y.-S. O3-Na-Fe$_{(1/3-x)}$Ni$_{1/3}$Mn$_{1/3}$Al$_x$O$_2$ Cathodes with Improved Air Stability for Na-Ion Batteries. *ACS Appl. Mater. Interfaces* **2021**, *13* (28), 33015−33023.

(19) Meng, X.; Zhang, D.; Zhao, Z.; Li, Y.; Xu, S.; Chen, L.; Wang, X.; Liu, S.; Wu, Y. O3-NaNi$_{0.47}$Zn$_{0.03}$Mn$_{0.5}$O$_2$ Cathode Material for Durable Na-Ion Batteries. *J. Alloys Compd.* **2021**, *887*, No. 161366.

(20) Yuan, X.-G.; Guo, Y.-J.; Gan, L.; Yang, X.-A.; He, W.-H.; Zhang, X.-S.; Yin, Y.-X.; Xin, S.; Yao, H.-R.; Huang, Z.; Guo, Y.-G. A Universal Strategy toward Air-Stable and High-Rate O3 Layered Oxide Cathodes for Na-Ion Batteries. *Adv. Funct. Mater.* **2022**, *32* (17), No. 2111466.

(21) Zheng, L.; Li, J.; Obrovac, M. N. Crystal Structures and Electrochemical Performance of Air-Stable Na$_{2/3}$Ni$_{1/3-x}$Cu$_x$Mn$_{2/3}$O$_2$ in Sodium Cells. *Chem. Mater.* **2017**, *29* (4), 1623−1631.

(22) Yao, H.-R.; Wang, P.-F.; Gong, Y.; Zhang, J.; Yu, X.; Gu, L.; OuYang, C.; Yin, Y.-X.; Hu, E.; Yang, X.-Q.; Stavitski, E.; Guo, Y.-G.; Wan, L.-J. Designing Air-Stable O3-Type Cathode Materials by Combined Structure Modulation for Na-Ion Batteries. *J. Am. Chem. Soc.* **2017**, *139* (25), 8440−8443.

(23) Wang, X.; Roy, S.; Shi, Q.; Li, Y.; Zhao, Y.; Zhang, J. Progress in and Application Prospects of Advanced and Cost-Effective Iron (Fe)-Based Cathode Materials for Sodium-Ion Batteries. *J. Mater. Chem. A* **2021**, *9* (4), 1938−1969.

(24) Kim, D.; Lee, E.; Slater, M.; Lu, W.; Rood, S.; Johnson, C. S. Layered Na [Ni$_{1/3}$Fe$_{1/3}$Mn$_{1/3}$]O$_2$ Cathodes for Na-Ion Battery Application. *Electrochem. Commun.* **2012**, *18*, 66−69.

(25) Yabuuchi, N.; Yano, M.; Yoshida, H.; Kuze, S.; Komaba, S. Synthesis and Electrode Performance of O3-Type NaFeO$_2$-NaNi$_{1/2}$Mn$_{1/2}$O$_2$ Solid Solution for Rechargeable Sodium Batteries. *J. Electrochem. Soc.* **2013**, *160* (5), A3131.

(26) Yuan, D. D.; Wang, Y. X.; Cao, Y. L.; Ai, X. P.; Yang, H. X. Improved Electrochemical Performance of Fe-Substituted Na-Ni$_{0.5}$Mn$_{0.5}$O$_2$ Cathode Materials for Sodium-Ion Batteries. *ACS Appl. Mater. Interfaces* **2015**, *7* (16), 8585−8591.

(27) Yao, H.-R.; Lv, W.-J.; Yin, Y.-X.; Ye, H.; Wu, X.-W.; Wang, Y.; Gong, Y.; Li, Q.; Yu, X.; Gu, L.; Huang, Z.; Guo, Y.-G. Suppression of Monoclinic Phase Transitions of O3-Type Cathodes Based on Electronic Delocalization for Na-Ion Batteries. *ACS Appl. Mater. Interfaces* **2019**, *11* (25), 22067−22073.

(28) Somerville, J. W.; Sobkowiak, A.; Tapia-Ruiz, N.; Billaud, J.; Lozano, J. G.; House, R. A.; Gallington, L. C.; Ericsson, T.; Häggström, L.; Roberts, M. R.; Maitra, U.; Bruce, P. G. Nature of the "Z"-Phase in Layered Na-Ion Battery Cathodes. *Energy Environ. Sci.* **2019**, *12* (7), 2223−2232.

(29) Li, X.; Wang, Y.; Wu, D.; Liu, L.; Bo, S.-H.; Ceder, G. Jahn−Teller Assisted Na Diffusion for High Performance Na Ion Batteries. *Chem. Mater.* **2016**, *28* (18), 6575−6583.

(30) Feng, Z.; Barai, P.; Gim, J.; Yuan, K.; Wu, Y. A.; Xie, Y.; Liu, Y.; Srinivasan, V. In Situ Monitoring of the Growth of Nickel, Manganese, and Cobalt Hydroxide Precursors During Co-Precipitation Synthesis of Li-Ion Cathode Materials. *J. Electrochem. Soc.* **2018**, *165* (13), A3077.

(31) Kresse, G.; Furthmüller, J. Efficiency of Ab-Initio Total Energy Calculations for Metals and Semiconductors Using a Plane-Wave Basis Set. *Comput. Mater. Sci.* **1996**, *6* (1), 15−50.

(32) Kresse, G.; Furthmüller, J. Efficient Iterative Schemes for Ab Initio Total-Energy Calculations Using a Plane-Wave Basis Set. *Phys. Rev. B* **1996**, *54* (16), 11169.

(33) Perdew, J. P.; Burke, K.; Ernzerhof, M. Generalized Gradient Approximation Made Simple. *Phys. Rev. Lett.* **1996**, *77* (18), 3865.

(34) Kresse, G.; Joubert, D. From Ultrasoft Pseudopotentials to the Projector Augmented-Wave Method. *Phys. Rev. B* **1999**, *59* (3), 1758.

(35) Dudarev, S. L.; Botton, G. A.; Savrasov, S. Y.; Humphreys, C.; Sutton, A. P. Electron-Energy-Loss Spectra and the Structural Stability of Nickel Oxide: An LSDA+U Study. *Phys. Rev. B* **1998**, *57* (3), 1505.

(36) Jain, A.; Hautier, G.; Ong, S. P.; Moore, C. J.; Fischer, C. C.; Persson, K. A.; Ceder, G. Formation Enthalpies by Mixing GGA and GGA+U Calculations. *Phys. Rev. B* **2011**, *84* (4), No. 045115.

(37) Yu, T.-Y.; Kim, J.; Hwang, J.-Y.; Kim, H.; Han, G.; Jung, H.-G.; Sun, Y.-K. High-Energy O3-Na$_{1−2X}$Ca$_X$[Ni$_{0.5}$Mn$_{0.5}$]O$_2$ Cathodes for Long-Life Sodium-Ion Batteries. *J. Mater. Chem. A* **2020**, *8* (27), 13776−13786.

(38) Kim, J. C.; Kwon, D.-H.; Yang, J. H.; Kim, H.; Bo, S.-H.; Wu, L.; Kim, H.; Seo, D.-H.; Shi, T.; Wang, J.; Zhu, Y.; Ceder, G. Direct Observation of Alternating Octahedral and Prismatic Sodium Layers in O3-Type Transition Metal Oxides. *Adv. Energy Mater.* **2020**, *10* (31), No. 2001151.

(39) Park, J.; Ku, K.; Son, S.-B.; Gim, J.; Kim, Y.; Lee, E.; Johnson, C. Effect of Electrolytes on the Cathode-Electrolyte Interfacial Stability of Fe-Based Layered Cathodes for Sodium-Ion Batteries. *J. Electrochem. Soc.* **2022**, *169* (3), No. 030536.

(40) Lee, E.; Brown, D. E.; Alp, E. E.; Ren, Y.; Lu, J.; Woo, J.-J.; Johnson, C. S. New Insights into the Performance Degradation of Fe-Based Layered Oxides in Sodium-Ion Batteries: Instability of Fe$^{3+}$/Fe$^{4+}$ Redox in α-NaFeO$_2$. *Chem. Mater.* **2015**, *27* (19), 6755−6764.

(41) Deng, C.; Gabriel, E.; Skinner, P.; Lee, S.; Barnes, P.; Ma, C.; Gim, J.; Lau, M. L.; Lee, E.; Xiong, H. Origins of Irreversibility in Layered NaNi$_x$Fe$_y$Mn$_z$O$_2$ Cathode Materials for Sodium Ion Batteries. *ACS Appl. Mater. Interfaces* **2020**, *12* (46), 51397−51408.

(42) Wang, X.; Ma, Y.; Raza, R.; Muhammed, M.; Zhu, B. Novel Core−Shell SDC/Amorphous Na$_2$CO$_3$ Nanocomposite Electrolyte for Low-Temperature SOFCs. *Electrochem. Commun.* **2008**, *10* (10), 1617−1620.

(43) Posada-Perez, S.; Rignanese, G.-M.; Hautier, G. Influence of Stacking on H$^+$ Intercalation in Layered ACoO$_2$ (A= Li, Na) Cathode Materials and Implications for Aqueous Li-Ion Batteries: A First-Principles Investigation. *Chem. Mater.* **2021**, *33* (17), 6942−6954.

(44) Cheng, C.; Hu, H.; Yuan, C.; Xia, X.; Mao, J.; Dai, K.; Zhang, L. Precisely Modulating the Structural Stability and Redox Potential of Sodium Layered Cathodes through the Synergetic Effect of Co-Doping Strategy. *Energy Storage Materials* **2022**, *52*, 10−18.

(45) Zhu, Y.-F.; Xiao, Y.; Dou, S.-X.; Chou, S.-L. Dynamic Structural Evolution and Controllable Redox Potential for Abnormal High-Voltage Sodium Layered Oxide Cathodes. *Cell Rep. Phys. Sci.* **2021**, *2* (11), No. 100631.